nature communications

Article

https://doi.org/10.1038/s41467-024-51570-9

Superlattice cathodes endow cation and anion co-intercalation for high-energy-density aluminium batteries

Received: 11 December 2023

Accepted: 8 August 2024

Published online: 16 September 2024

Check for updates

Fangyan Cui[1], Jingzhen Li[2], Chen Lai[1], Changzhan Li[1], Chunhao Sun[1], Kai Du[1], Jinshu Wang[1], Hongyi Li[1,3] ✉, Aoming Huang[4], Shengjie Peng[4] ✉ & Yuxiang Hu[1] ✉

Conventionally, rocking-chair batteries capacity primarily depends on cation shuttling. However, intrinsically high-charge-density metal-ions, such as Al^{3+}, inevitably cause strong Coulombic ion-lattice interactions, resulting in low practical energy density and inferior long-term stability towards rechargeable aluminium batteries (RABs). Herein, we introduce tunable quantum confinement effects and tailor a family of anion/cation co-(de)intercalation superlattice cathodes, achieving high-voltage anion charge compensation, with extra-capacity, in RABs. The optimized superlattice cathode with adjustable van der Waals not only enables facile traditional cation (de)intercalation, but also activates O^{2-} compensation with an extra anion reaction. Furthermore, the constructed cathode delivers high energy-density (466 Wh kg^{-1} at 107 W kg^{-1}) and one of the best cycle stability (225 mAh g^{-1} over 3000 cycles at 2.0 A g^{-1}) in RABs. Overall, the anion-involving redox mechanism overcomes the bottlenecks of conventional electrodes, thereby heralding a promising advance in energy-storage-systems.

The growth of large-scale lithium-ion batteries (LIBs) has been constrained by limited lithium reserves with high cost, uneven distributions, and safety concern[1,2]. Rechargeable aluminium batteries (RABs) have attracted global interest in the "beyond-lithium" energy landscope, owing to their relatively low prices, abundant resources, and high safety[3,4]. However, a significant obstacle to the scalable development of RABs arises from the high-charge-density of aluminium ions (Al^{3+}, 364 C mm^{-3}) with robust Coulombic ion-lattice interactions, which severely hamper long-term stability of RABs[5]. More seriously, the capacity of conventional rocking-chair RABs electrodes primarily relies on single-cation (Al^{3+}) shuttling and suffers from low practical capacity and strong lattice stress. Therefore, activating extra-anion shuttling is promising for the development of multivalent-ion batteries.

Previously, considerable efforts of the single anion (typically $AlCl_4^-$) insertion/extraction in graphite materials have been proposed in RABs, although the reported cathodes own inherently limited capacity (usually <150 mAh g^{-1})[6,7]. This constraint prompted us to explore cation and anion co-(de)intercalation in transition metal chalcogenides (TMCs) cathodes with intrinsically high theoretical capacity, such as V_2O_5[8]. However, strong electrostatic repulsive forces and inherent lattice stress limit the efficient uptake and removal of large anions from conventional metal oxides. In particular, long-range periodic superlattice configurations hold promise as they open up unique avenues for altering electronic properties, particularly van der Waals (vdW) forces[9,10]. The construction of superlattice materials is a facile approach for initiating extra anion charge

[1]Key Laboratory of Advanced Functional Materials, College of Materials Science and Engineering, Beijing University of Technology, Beijing 100124, P. R. China. [2]Key Laboratory of Optoelectronics Technology, Ministry of Education, Faculty of Information Technology, Beijing University of Technology, Beijing 100124, China. [3]College of Carbon Neutrality Future Technology, Beijing University of Technology, Beijing 100124, P. R. China. [4]College of Materials Science and Technology, Nanjing University of Aeronautics and Astronautics, Nanjing 210016, China. ✉e-mail: lhy06@bjut.edu.cn; pengshengjie@nuaa.edu.cn; y.hu@bjut.edu.cn

compensation reactions, in which the lattice O^{2-} can be activated in oxide electrodes. As expected, superlattice TMC cathodes would be promising for the development of response mechanisms with cation and anion co-(de)intercalation redox chemistry, as yet unreported in RABs technology.

Herein, we propose a family of cation/anion co-(de)intercalation superlattice cathodes in RABs, featuring extra anion redox reactions and high potential (above 2.0 V) via tunable quantum confinement effects. The optimized superlattice polyaniline-decorated vanadium pentoxide (P-V_2O_5) cathode substantially tunes the interlayer vdW forces, pioneering the extra-anion-participating mechanism in TMCs for RAB with an ultrahigh energy density (466 Wh kg^{-1} at 107 W kg^{-1}). Compared with conventional cathodes, such as V_2O_5, the superlattice cathodes (P-V_2O_5) enable the Al^{3+} and $AlCl_4^-$ co-(de)intercalation via activating extra O^{2-} redox reactions, which is verified by theoretical simulations and a series of in/ex-situ characterizations. Meanwhile, the superlattice crystalline structure provides a suitable balance between stress concentration and volume expansion from the high-charge-density Al^{3+} and the large-sized $AlCl_4^-$. Thus, the well-designed P-V_2O_5 achieves one of best long-term stabilities (225 mAh g^{-1} at 2.0 A g^{-1} over 3000 cycles) in metal-chalcogenide cathodes. Overall, the proposed cation and anion co-(de)intercalation behavior in superlattice cathodes would provide feasible avenues for high-performance multivalent-ion batteries.

Results

Structural evolution from traditional oxides to superlattice

To verify the above hypothesis towards extra $AlCl_4^-$ intercalation in superlattice materials, superlattice polyaniline-decorated vanadium pentoxide (P-V_2O_5) with various equivalents of polyaniline (PANI) molecules was optimized as a model superlattice cathode. Driven by Coulombic forces, organic melocules were intercalated to form a superlattice structure with periodic variations. The phases and structures of the samples are studied using X-ray diffraction (XRD) and Rietveld analysis (Fig. 1a). Rietveld refinements revealed that the calculated results were similar to the experimental data, with properly fitted *R*-value (R_e = 0.83%, R_{wp} = 3.64%, and R_p = 2.75%). Furthermore, after the intercalation of the aniline molecules, a noticeable shift towards lower angles was observed for all (00 l) peaks in the as-prepared superlattice P-V_2O_5, indicating an expansion of the V_2O_5 layers and an increase in the *c*-axis lattice constant. The *c*-axis lattice constant, that is, the interlayer distance, was calculated to be 13.81 Å. In contrast, the pristine V_2O_5 crystal exhibits only the orthorhombic space group (pmmn), and the strong (00 l) peaks are perpendicular to the basal plane (Supplementary Fig. 1). Thus, a graphite-like bilayer structure forms as organic molecules intercalate into the interlayers of vanadium-based electrodes. A typical superlattice crystal structure with an expanded interlayer is shown in Fig. 1b. Appropriate aniline inlays are significant for forming an effective superlattice

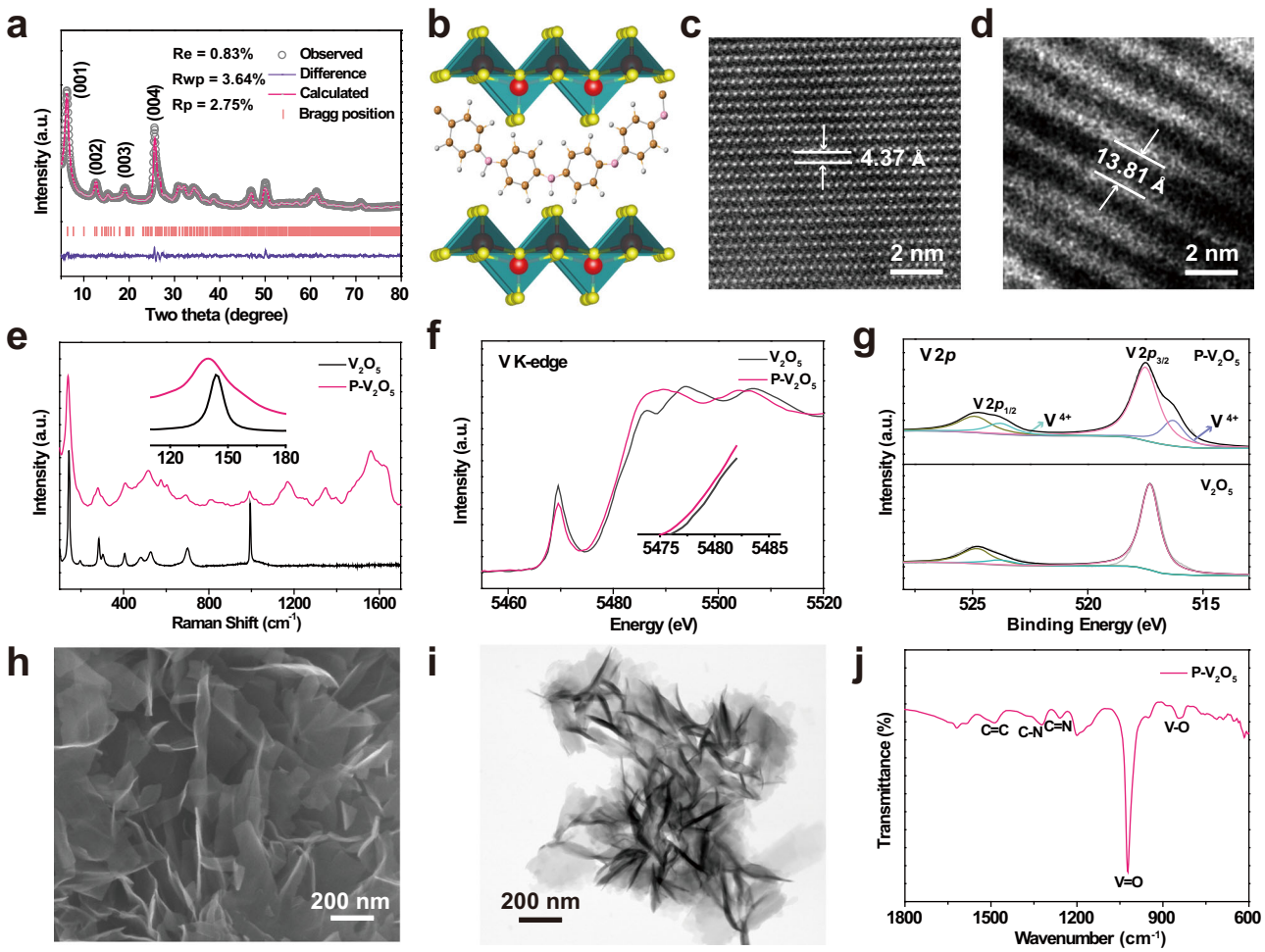

Fig. 1 | Physicochemical characterizations of the as-prepared superlattice P-V_2O_5 and conventional V_2O_5. a X-ray diffraction (XRD) patterns and Rietveld plots of P-V_2O_5. **b** Corresponding superlattice crystal structure. The high-resolution cross-sectional transmission electron microscopy (TEM) images of c, V_2O_5 and d, P-V_2O_5. **e** Raman spectra of pristine V_2O_5 and superlattice P-V_2O_5. **f** Normalized X-ray absorption near edge structure (XANES) spectra for V K-edge of P-V_2O_5 and pristine V_2O_5. **g** X-ray photoelectron spectroscopy (XPS) spectra of P-V_2O_5 and pristine V_2O_5. **h** Scanning electron microscopy (SEM) image of P-V_2O_5. **i** TEM image of P-V_2O_5. **j** Fourier transform infrared (FT-IR) spectra of P-V_2O_5.

configuration (Supplementary Fig. 2). The excess intercalated molecules show an inhomogeneous distribution in the scanning electron microscopy (SEM) images (Supplementary Fig. 3), which is attributed to the spatially varied distribution of the protonated long-chain PANI in the hybrid species. Moreover, cross-sectional transmission electron microscopy (TEM) images show a distinct structural discrepancy between the conventional V_2O_5 and the superlattice P-V_2O_5 (Fig. 1c, d). The TEM results revealed a significant interlayer distance expansion from 4.37 Å in pristine V_2O_5 to 13.81 Å in superlattice P-V_2O_5, which was consistent with the XRD results. The increased interlayer distance (~9.44 Å) roughly corresponded to the polymerization degree of protonated polyaniline with oxidation and reduction substituents. Thermogravimetric analysis (TGA) exhibits that the PANI in P-V_2O_5 is 9.70% with 2.10% crystalline water, indicating that besides V_2O_5 the coexistence of polyaniline and tightly bound water in the superlattice structure (Supplementary Fig. 4). Raman spectra present a slight red-shifted of the external [VO_5]–[VO_5] modes from V_2O_5 (143.7 cm^{-1}) to superlattice P-V_2O_5 (139.5 cm^{-1}) (Fig. 1e). The Raman evolutions indicate the lower energies and local disorder phenomenon in the superlattice configuration, the possible strain-induced bandgap transformation, and weak vdW forces[11]. Furthermore, compared to the conventional V_2O_5 material, the V K-edge of superlattice P-V_2O_5 shifts toward lower energy via X-ray absorption near edge structure (XANES), implying a lower average valence state in superlattice P-V_2O_5 (Fig. 1f). The Fourier transformation (FT) of the extended X-ray absorption fine structure (EXAFS) spectra further confirm the differences between the samples (Supplementary Fig. 5). The FT peaks of V_2O_5 (around 1.53/2.61 Å) and P-V_2O_5 (around 1.56/2.64 Å) corresponded to the O atom from the absorbed V (V-O distances). The incremental radial distance of V-O in P-V_2O_5 suggested that the P-V_2O_5 exhibited weaker vdW forces than that of V_2O_5, which was similar to the Raman result[12]. Thus, compared to conventional crystal V_2O_5, the superlattice P-V_2O_5 exhibited a certain disorder in layer structure.

Notably, the X-ray photoelectron spectroscopy (XPS) characterization of V 2*p* spectra shows that the superlattice P-V_2O_5 exhibits a lower valence state (V^{4+}) than V_2O_5 (Fig. 1g), which is mainly ascribed to its unique structure. XPS analysis further delivers the presence of O 1*s*, C 1*s*, and N 1*s* elements in the superlattice P-V_2O_5, indicating the successful introduction of PANI (Supplementary Fig. 6). The SEM images (Fig. 1h and Supplementary Fig. 7) display that the optimized superlattice P-V_2O_5 maintains an ultrathin and uniform nanosheet morphology. Compared with traditional bulk V_2O_5 (Supplementary Fig. 7a), superlattice P-V_2O_5 with a layered nanosheet structure has more active sites with accelerated ion and electron transport[13]. The TEM images also confirm the homogeneous lamellar structure of P-V_2O_5 (Fig. 1i and Supplementary Fig. 8). Atomic force microscopy (AFM) results reveal a thickness distribution of ~3.7 nm, indicating the presence of a considerably nanoscale thin layer structure (Supplementary Fig. 9). The surface potential of V_2O_5 and P-V_2O_5 was 0.62 and 0.64 V based on a Kelvin probe force microscopy (KPFM) test, respectively. Compared with conventional V_2O_5, the superlattice P-V_2O_5 has a larger work function, which attracts the electron cloud of molecules and accelerates the interfacial charge transfer[14]. The sheet resistance test (Supplementary Fig. 10) also demonstrates the enhanced electron conductivity that P-V_2O_5 exhibits a resistance value (1.10 kΩ $\square^{-1}$) in comparion with the pure sample (3.62 kΩ $\square^{-1}$). Fourier transform infrared (FT-IR) spectroscopy further demonstrates that superlattice P-V_2O_5 retains the respective characteristics of V_2O_5 crystals and PANI molecules (Fig. 1j)[15].

As a certain system extension, several superlattice cathodes were also prepared, including, hexadecyl trimethyl ammonium bromide decorated vanadium pentoxide (V_2O_5-CTAB), sodium dodecyl benzene sulfonate modified V_2O_5 (V_2O_5-SDBS), and polyaniline-inserted molybdenum trioxide (P-MoO_3). The XRD pattern of the designed V_2O_5-CTAB shows that an interlayer distance expansion and periodic diffraction peaks (Supplementary Fig. 11a). Furthermore, P-MoO_3 and V_2O_5-SDBS exhibit similar XRD evolutions as the optimized superlattice P-V_2O_5 (Supplementary Fig. 11b, c). Consequently, the intermolecular intercalation of certain organic ligands promoted the formation of a superlattice structure. The soft organic capping ligand presented strong interactions and self-organization, which were conducive to decoupling the interlayer interactions. Superlattice materials with tunable intermolecular forces are promising for coping with high-charge-density Al ions and achieving extra-anionic redox reactions.

Simulated anion storage behavior of superlattice cathodes in RABs

To explore the potential of extra-anion in the as-prepared superlattice cathodes in RABs, series of simulations were conducted towards P-V_2O_5 and conventional V_2O_5. Owing to the inherently strong cation lattice interactions in rocking-chair multivalent-ion battery chemistry, such as the interactions with trivalent aluminium ions (Al^{3+}, 364 C mm^{-3}), conventional cathodes exhibit a large overpotential and sluggish kinetics, leading to practical voltage hysteresis and inferior battery stability[16]. The (de)intercalation of high-charge-density Al^{3+} usually causes an irreversible collapse of the host structure and a large intercalation barrier, resulting in inferior cycling stability and insufficient capacity (Fig. 2a). The proposed extra anionic redox reactions in superlattice materials would further improve the practical capacity of RABs (Fig. 2b). Note that, the insertion/extraction of extra anions would generate extra platform. The output voltage (V_c) of the RABs was positively correlated with the intercalation energy (IE), which was influenced by the interaction between the anions and the host matrix. Moreover, only a suitable IE can activate anion redox reactions. Previously, large polarization existed in the reported TMCs electrodes for RABs[17,18], which hardly achieved anionic shuttling. Compared to the conventional electrodes, the family of superlattice materials with ultra-stable structure have the potential to achieve reversible Al^{3+} and $AlCl_4^-$ shuttling (Fig. 2b). As shown in Fig. 2c, the energy barriers between the isolated ions and the intercalant states are in suitable cathodes. Notably, the IE of $AlCl_4^-$ negatively was related to the Gibbs free energy (ΔG), and thus determined the electrode voltage of RABs.

The anion intercalation into superlattice P-V_2O_5 behavior was investigated in this work via density functional theory (DFT) calculations. The calculation results revealed that the superlattice cathode could process the action of suitable $AlCl_4^-$ ions intercalation with appropriate IE and potential. Specifically, the optimal tetrahedral configuration of $AlCl_4^-$ in layered superlattice systems was stable. Thus, a configuration similar to that reported graphite-based systems was adopted to conduct the simulations[19]. Different specific intercalation stages are simulated; the optimized structure of $AlCl_4^-$ intercalation process is shown in Supplementary Fig. 12. The calculated results reveal that the [$(AlCl_4)_x$(P-V_2O_5)] compounds exhibit a certain amount of $AlCl_4^-$ intercalation (the simulated 1, 2, and 3 stages), corresponding to the discrepant voltages of 2.03, 1.53, and 0.83 V, respectively (Fig. 2d and Supplementary Tables 1, 2). Note that, this simulation is aimed to estimate the anion intercalation capacity of P-V_2O_5. Ion diffusion behavior plays a crucial role in the electrochemical performance of batteries. The barriers for $AlCl_4^-$ diffusing in superlattice P-V_2O_5 and conventional V_2O_5 were simulated. The low diffusion energy barrier in superlattice P-V_2O_5 indicates that the ions diffuse within the lattice much more easily than in V_2O_5 (Supplementary Fig. 13). The superlattice P-V_2O_5 keep stable geometric structure under the large-sized $AlCl_4^-$ (Supplementary Fig. 14). However, the conventional crystal V_2O_5 with limited interlayer spacing (4.37 Å) exhibits a certain local strain (Supplementary Fig. 15 and Supplementary Table 3). Based on previous research of the barrier calculation, the practical disordered P-V_2O_5 presented lower values than the simulated crystal structure[20,21]. Furthermore, the finite

https://doi.org/10.1038/s41467-024-51570-9

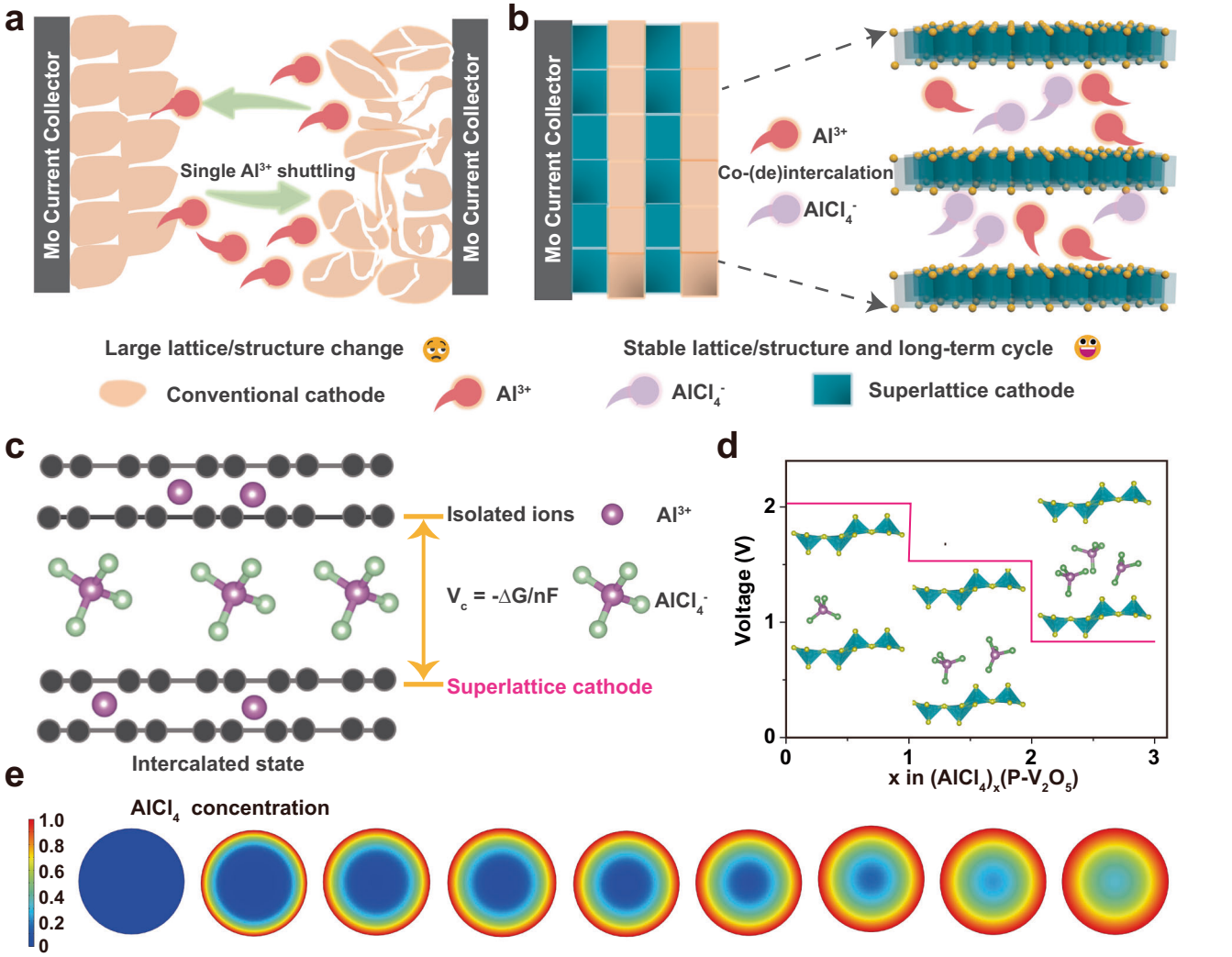

Fig. 2 | Exploration of extra-anion transportation in superlattice P-V_2O_5 in RABs. Schematic illustrations of (**a**) cation (Al^{3+}) shuttling in conventional cathodes and (**b**) the anion ($AlCl_4^-$) and cation (Al^{3+}) co-(de)intercalation in superlattice electrodes; the superlattice cathode exhibits more stable structure than the conventional electrode. **c** Schematic process of active ions intercalating into designed superlattice cathode with corresponding energy barriers. **d** Simulated voltage profile of extra anion inserted into P-V_2O_5 system. **e** Finite element simulation of anion diffusion in superlattice P-V_2O_5.

element analysis reveals a continuum $AlCl_4^-$ diffusion in the superlattice P-V_2O_5 (Fig. 2e). In the P-V_2O_5, with the evolution time increasing, the $AlCl_4^-$ diffuses from the ion-rich outer layer to the poor inner layer (Supplementary Video 1). Notably, superlattice electrodes presented snapshots of simulated $AlCl_4^-$ distribution and tolerable volume expansion. Superlattice P-V_2O_5 enhanced $AlCl_4^-$ dynamics transport in the RABs and made anion/cation co-(de)intercalation possible. Overall, these calculation results for the superlattice cathode materials provide further kinetics insights into achieving extra anion (de)intercalation electrodes.

Stability of superlattice cathode under cation/anion co-(de) intercalation

To further confirm that the extra anionic diffusion thermodynamical capable of superlattice cathodes, adsorption energy calculations were performed. The large adsorption energy proves that the superlattice P-V_2O_5 has a stronger $AlCl_4^-$ attraction than pristine V_2O_5 and polyaniline, resulting in enhanced $AlCl_4^-$ intercalation into the lattice (Fig. 3a and Supplementary Table 4). Furthermore, differential charge density calculations reveal that the O on V_2O_5 before adsorption is negatively charged and the charge density is electron-dense (Fig. 3b; pink is the electron-dense region, and yellow is the electron-deficient region). After adsorption, the O of pristine V_2O_5 had a few yellow regions, indicating that particle charge was transferred to anion ($AlCl_4^-$). In particular, most of the O in the superlattice P-V_2O_5 was an electron-dense (pink) region, signifying the strong interaction between superlattice P-V_2O_5 and $AlCl_4^-$. These results were consistent with the absorption energy calculations. Thus, these calculations for the superlattice cathode materials provided insights towards achieving extra anion (de)intercalation and high-stability electrodes. The experimental cyclic voltammetry (CV) curve of the P-V_2O_5 cathode also indicates a high oxidation peak (above 2.0 V) in the RABs (Fig. 3c), which is consistent with the theoretical results. Therefore, the superlattice P-V_2O_5 electrodes own the potential to realize extra $AlCl_4^-$ redox reaction with additional high voltage. Particularly, the extra anion-participating redox mechanism is different from that of single Al^{3+} (de) intercalation in conventional TMC electrodes[22]. To verify the structural stability of superlattice materials under the intercalation process of large active ions, the XRD pattern shows that the superlattice cathode presents an intact crystal structure (Supplementary Fig. 16). Furthermore, finite element analysis reveals a chemomechanical simulation of the superlattice P-V_2O_5 via the elastoplastic deformation equation (Fig. 3d). As the evolution time increases, the associated von Misses stress is redistributed in the P-V_2O_5 model (Supplementary Video 2).

https://doi.org/10.1038/s41467-024-51570-9

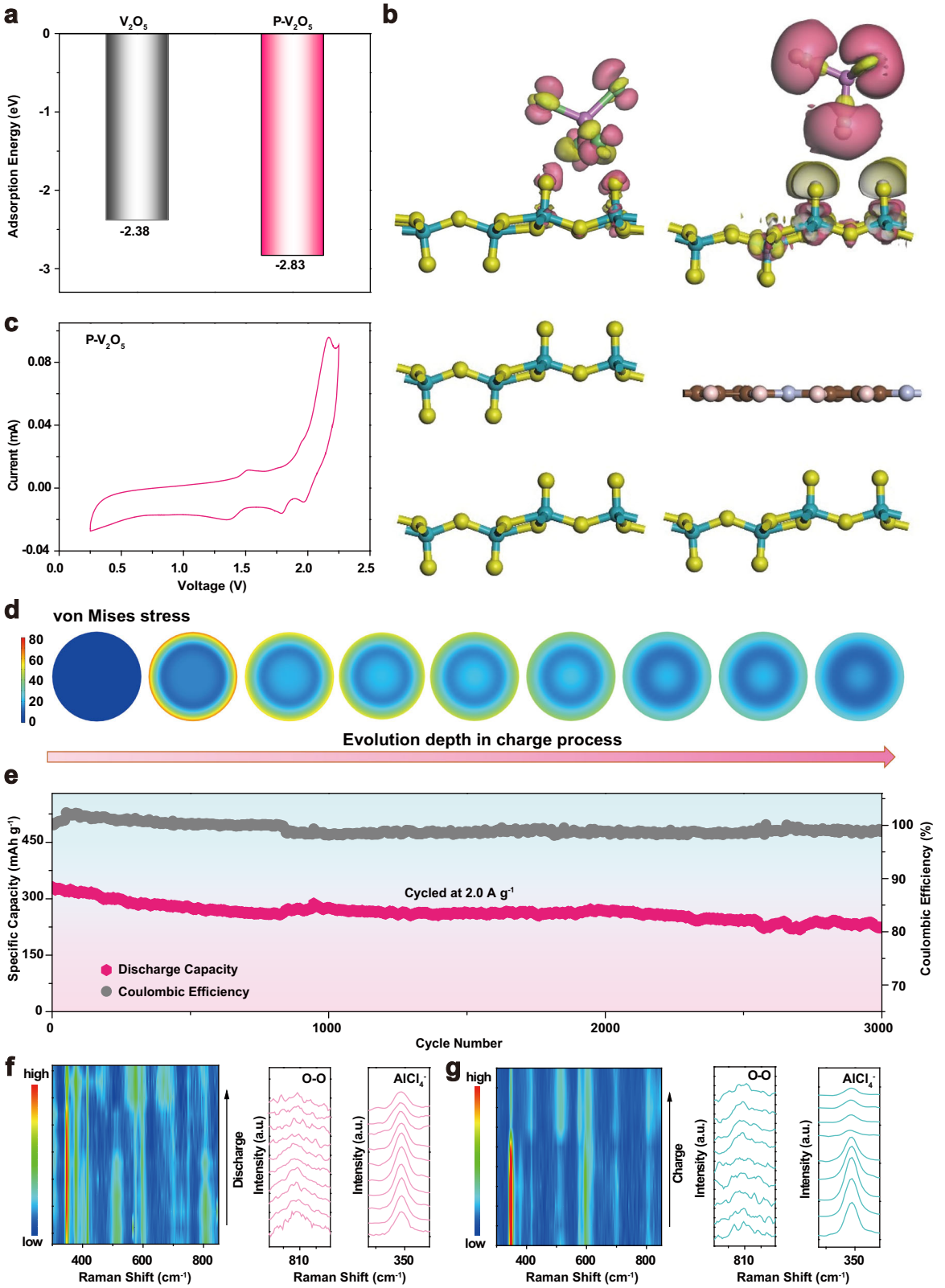

Fig. 3 | Investigation of structural stability of P-V_2O_5 with in-situ characterization. a Calculated adsorption energy of $AlCl_4^-$ intercalation of the conventional V_2O_5 and superlattice P-V_2O_5. **b** Differential charge density of pristine V_2O_5 and superlattice P-V_2O_5. **c** Experimental cyclic voltammetry (CV) curves for designed superlattice P-V_2O_5 cathode. **d** Finite element simulation of von Mises stress distribution in superlattice P-V_2O_5. **e** Long-term cycling of P-V_2O_5 at a high current density of 2.0 A g^{-1}. In-situ Raman spectra for (**f**), the discharging process with the related magnified O-O, and $AlCl_4^-$ spectral profiles, and (**g**) charging process with the related magnified O-O, and $AlCl_4^-$ spectral profiles.

Notably, the superlattice electrodes presented snapshots of the simulated radial stress distribution, and both volume expansion and stress concentration were well balanced. The lattice structural stability improved the long-term cycling performance of the optimized P-V_2O_5. Moreover, the superlattice P-V_2O_5 cathode exhibits a high capacity and long-term stability even at a high currernt density (225 mAh g^{-1} over 3000 cycles at 2.0 A g^{-1}, Fig. 3e and Supplementary Fig. 17), which is far superior to that of conventional V_2O_5 (Supplementary Fig. 18). The long-term stability is also related to the side reactions with the binder and current collector in the Lewis acidic electrolyte system (Supplementary Fig. 19)[23]. Furthermore, both the P-MoO_3 and V_2O_5-CTAB superlattice cathodes exhibit remarkable cycling stabilities (Supplementary Fig. 20).

To reveal the extra anion-involving redox mechanism in superlattice P-V_2O_5 electrode and gain a deeper understanding of the structural transformation, a real-time Raman spectroscopy was performed. The low-wavenumber strong peak corresponds to the external [VO_5]–[VO_5] modes, signifying the stable long-range order structures (Supplementary Fig. 21). Particularly, the [VO_5] polyhedron shows a slightly weak evolution at the initial discharge plateau (~1.80 V) until a Raman signal (179 cm^{-1}) appears after further deep discharging, which is attributed to lattice distortion from ample active ion intercalation (Supplementary Fig. 21a). Notably, the representative V-O (513 cm^{-1}) and O-O (~808 cm^{-1}) vibrations also radically reduce, which further confirms the participation of extra anion $AlCl_4^-$ during the discharge process (Fig. 3f and Supplementary Fig. 22). In addition, the signal of $AlCl_4^-$ at 349 cm^{-1} exhibited an initial enhancement followed by a decreasing trend, which was attributed to the release of $AlCl_4^-$ during preliminary discharge (above 1.80 V) and subsequent further insertion of Al^{3+}. The charging process exhibited good reversibility for the superlattice P-V_2O_5 cathode. The contour diagram indicates the reversible transformation of the V-O and O-O stretching vibrations during charging (Fig. 3g). Moreover, $AlCl_4^-$ signal also presented the reverse Raman variation during charging as compared to the discharge process. The slightly distorted [VO_5] polyhedra are gradually recovered (Supplementary Fig. 21b). The peaks from 1000 cm^{-1} to 1600 cm^{-1}, belonging to polyaniline, show limited variation during the discharge-charge process (Supplementary Fig. 23). Raman vibrations of $AlCl_4^-$ and O-O provided adequate evidence of the cationic and anionic co-(de)intercalation in the superlattice P-V_2O_5 cathode. In contrast, Raman signals of conventional V_2O_5 cathode exhibit only the single V-O transformation (Supplementary Fig. 24) except for the unique $AlCl_4^-$ and O-O evolutions in the optimized P-V_2O_5.

To further understand the unique two-step electrochemical behavior and confirm the extra anionic redox mechanisms to superlattice materials, the P-V_2O_5 electrodes were investigated in details via series of characterizations. The electrodes at representative stages (Supplementary Fig. 25) are adequately washed to eliminate surplus electrolytes, and then dried under Ar protection. Supplementary Fig. 26a exhibits the V 2*p* XPS profiles of the P-V_2O_5 electrode at typical stages, that is, pristine, discharged to 1.80 V, fully discharged (0.25 V), charged to 2.05 V, and fully charged (2.25 V). At the pristine state, the peaks located at 517.40 eV, 516.30 eV (V $2p_{3/2}$), and 524.85 eV, 523.65 eV (V $2p_{1/2}$) were ascribed to V^{5+} and V^{4+}, respectively. The weak V^{4+} peaks were attributed to the reduction in protonated polyaniline during superlattication. When the electrode was discharged to 1.80 V, the V 2*p* peak barely changed. After discharge to 0.25 V, the peak intensity of V^{5+} decreased, whereas that of the V^{4+} peak increased. More prominently, a lower binding energy V 2*p* peaks appeared (located at 522.80 and 515.30 eV, respectively), resulting from the Al-based active ion insertion. After the electrode was fully charged to 2.05 V, the V 2*p* peak recovered to high binding energy, confirming the reversibility between the Al-based active ions and P-V_2O_5 during the electrochemical reaction process. Moreover, there was negligible variation in the V 2*p* peak while charging from 2.05 to 2.25 V. This slight change in the V 2*p* specrta in the initial discharge (~1.80 V) and high charge potential region (above 2.05 V) during the entire discharging/charging process was different from that of conventional V_2O_5[22]. Note that, the O 1*s* depth-profiling XPS analysis presents remarkable evolution (a peak appears at ~531.20 eV) after discharging to 1.80 V and charging to 2.05 V, suggesting the existence of the O^- species or other coordinated oxidized oxygen (Supplementary Fig. 26b). Unlike the XPS behavior of conventional V_2O_5, the O^{2-}/O^- transformation in P-V_2O_5 acted as a charge compensation during charge/discharge process, confirming the (de)intercalation of $AlCl_4^-$. The etching O 1*s* XPS spectra show the presence of O^-/O_n^{n-} in the P-V_2O_5 electrode under different etching times (30 and 60 s) when charged to 2.05 V (Supplementary Fig. 27). Moreover, the evolutions of the XPS spectra of Al 2*p* and Cl 2*p* further indicate the Al^{3+} and $AlCl_4^-$ insertion/extraction during the entire electrochemical process (Supplementary Fig. 28). Furthermore, the ex-situ TEM-energy dispersive spectroscopy (TEM-EDS) mapping images of superlattice P-V_2O_5 cathodes indicates the evolutions of Al-ion and $AlCl_4^-$, the P-V_2O_5 electrode maintains structural integrity (Supplementary Fig. 29). Thus, accompanying extra $AlCl_4^-$ (de)intercalation of the superlattice-type RABs system, the variations of observed peroxo-like species preserved the charge compensation. In this case, we proposed the Al^{3+} and $AlCl_4^-$ co-(de) intercalation reaction mechanism for RABs in the model superlattice P-V_2O_5 electrode. The charge electrochemical reactions in RABs are divided into two independent processes, including the removal of Al^{3+} and the uptake of $AlCl_4^-$ (Supplementary Fig. 30). Consequently, the process of cationic and anionic co-(de)intercalation was expounded and the reversibility of the unique extra-anion-paticipating redox mechanism was verified for superlattice materials in RABs.

Electrochemical performance of superlattice cathode

Following the characterization and simulation towards superlattice P-V_2O_5, the electrochemical performance of the P-V_2O_5 in RABs was further evaluated. In the CV curves, there are discrepant redox peaks in the voltage range from 0.25–2.25 V at a scan rate of 0.50 mV s^{-1} (Fig. 4a). One peak at 1.46 V and another distinct peak at around 2.16 V during the oxidation reaction was observed, which indicated a two-step process of Al-based active ion storage in the P-V_2O_5 electrode. The corresponding reduction peaks were shown at 1.21 and 1.79 V. Additional, minor reduction and oxidation peaks observed at high potential may be attributed to side reactions occurring in the electrolyte. On the contrary, the Al/V_2O_5 battery only had one pair of weak redox peaks in the low-voltage region, which was attributed to the single Al-ions (de) intercalation[22]. Notably, the superlattice P-V_2O_5 maintains a stable open circuit voltage in comparision with that of conventional V_2O_5 (Supplementary Fig. 31). Furthermore, the CV curves of protonated polyaniline (PANI-H) reveal two pairs of reduction and oxidation peaks at ~1.05/1.66 V and 1.13/1.75 V (Supplementary Fig. 32), which is consistent with the previously reported work[24]. Based on the above results, superlattice P-V_2O_5 showed an abnormal redox peaks (above 2.0 V), indicating that the developed cathodes involved a revolutionary redox reaction mechanism. Meanwhile, several well-designed superlattice cathodes (V_2O_5-CTAB, V_2O_5-SDBS, and P-MoO_3) show similar redox behaviors in RABs (Supplementary Fig. 33). Furthermore, the superlattice P-V_2O_5 exhibits a reversible capacity of 436 mAh g^{-1} at 100 mA g^{-1} after the initial activation, more than two times higher than that of conventional V_2O_5 (177 mAh g^{-1} at 100 mA g^{-1}, Fig. 4b and Supplementary Fig. 34). Moreover, the superlattice P-V_2O_5 presents a high average discharge voltage of 1.07 V and reduced overpotential (Supplementary Fig. 35). Accordingly, the superlattice cathode possessed high potential and energy density (466 Wh kg^{-1} at 107 W kg^{-1}). Besides, a series of hybrid P_x-V_2O_5 and blended V_2O_5@PANI electrodes exhibit comparatively low capacities (Supplementary Fig. 36). The conductive agent (Ketjenblack, KB) in cathode has a negligible capacity (Supplementary Fig. 37a). The capacity of the PANI-H cathode is

https://doi.org/10.1038/s41467-024-51570-9

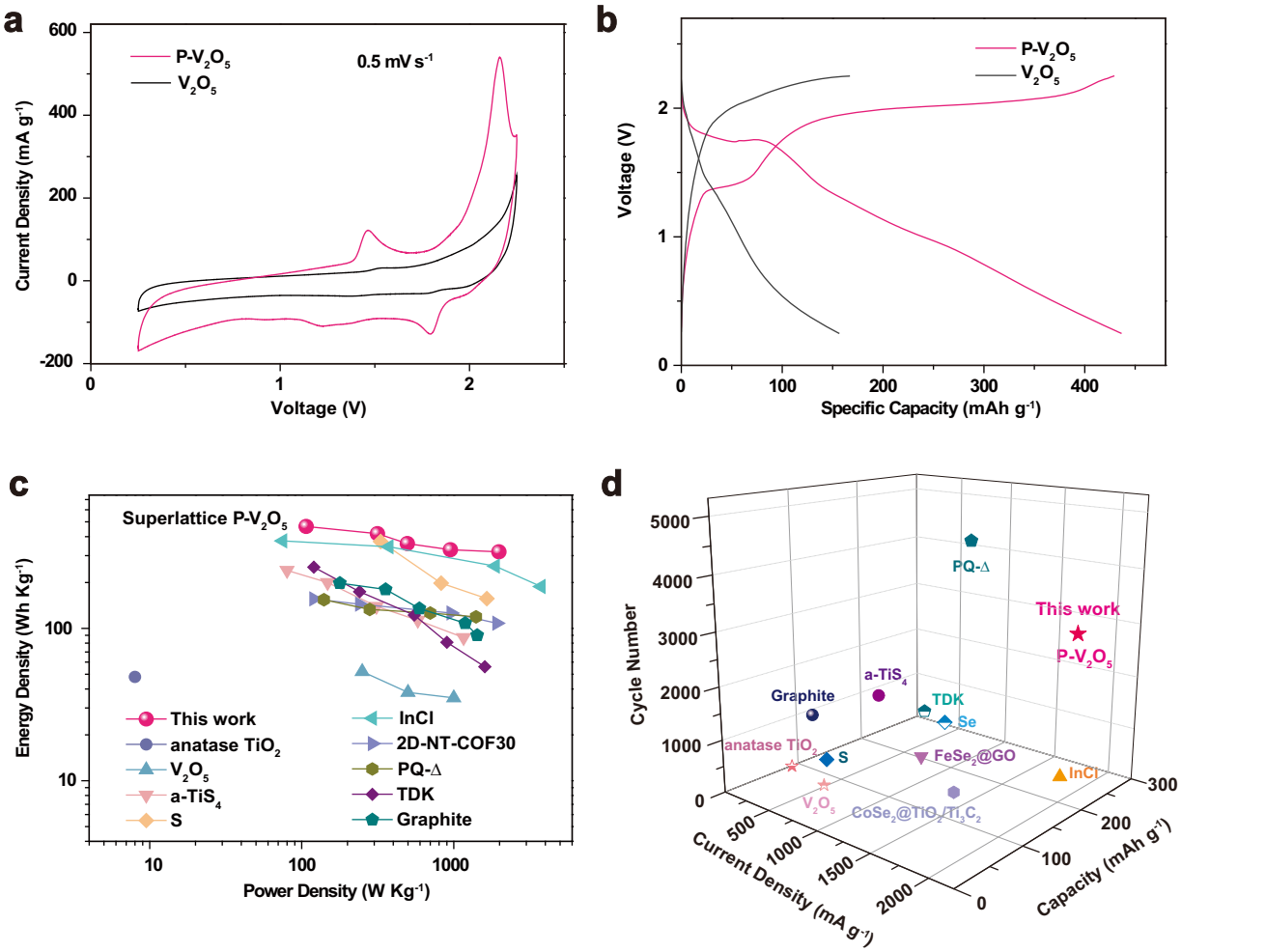

Fig. 4 | Electrochemical performance of superlattice P-V_2O_5 in RABs. a CV profiles of superlattice P-V_2O_5 and conventional V_2O_5 at a scan rate of 0.5 mV s^{-1}. **b** Discharge-charge curves of P-V_2O_5 and V_2O_5 at 100 mA g^{-1}. **c** Ragone plot of P-V_2O_5 and representative cathodes in RABs[25–33]. **d** Long-term stability of P-V_2O_5 and representative cathodes materials in RABs[25–28,30–36].

also much lower than that of the superlattice P-V_2O_5 (Supplementary Fig. 37b). Considering the contribution of the intermolecular PANI, the practical capacity of P-V_2O_5 exceeded the theoretical capacity of V_2O_5 (single cations (Al-ions) shuttling), which also confirmed the extra anionic redox mechanism in superlattice cathodes. Moreover, the superlattice P-V_2O_5 cathode exhibits one of the highest energy density among the reported representative cathode materials in RABs (318 Wh kg^{-1} at a power density of 1980 W kg^{-1}) (Fig. 4c and Supplementary Table 5)[25–33], which is ascribed to the facile ion/electron diffusion in superlattice electrodes.

The P-V_2O_5 sample presented a reduced voltage gap compared to that of pristine V_2O_5 via galvanostatic intermittent titration technique (GITT) measurements, suggesting an enhanced kinetic process (Supplementary Fig. 38). Compared with the average diffusion coefficient of Al-based ions in the V_2O_5 sample ($10^{-13.57}$ cm^2 s^{-1}), the P-V_2O_5 exhibits significant improvement ($10^{-11.44}$ cm^2 s^{-1}, Supplementary Fig. 39). To the best of our knowledge, the life-span of P-V_2O_5 is the highest and the capacity remained 225 mAh g^{-1} at 2.0 A g^{-1} over 3000 cycles among oxide-based cathodes in RABs (Fig. 4d and Supplementary Table 6)[25–28,30–36], which is mainly ascribed to the unique superlattice structure and cationic (Al^{3+}) and anionic ($AlCl_4^-$) co-(de) intercalation mechanism. Therefore, the reversible extra anionic redox reactions are achieved towards superlattice cathodes for high-performance RABs, particularly the extra-high capacity and long-term stability.

Discussion

In summary, distinguished from conventional cathode materials, we propose an unexplored superlattice cathodes (P-V_2O_5) for RABs with unique anion/cation co-(de)intercalation mechanism. Verifying by theoretical simulations and corresponding experiments, besides the conventional cationic ($V^{5+} \leftrightarrow V^{3+}$) reversible evolution, the sub-participation of anion-redox ($O^{2-} \leftrightarrow O^{-}/O_n^{n-}$) in the optimized superlattice cathode significantly increased, resulting in superior capacity (436 mAh g^{-1} at 100 mA g^{-1}). Furthermore, the robust superlattice crystalline structure is especially favor to the high-charge-density Al^{3+} and large-sized $AlCl_4^-$ in RABs, which contributes to one of the best long-term stabilities (225 mAh g^{-1} at a high current density of 2.0 A g^{-1} over 3000 cycles) among reported cathodes in RABs. Overall, we believe that the advancement of extra-anion redox-participating electrode materials, such as superlattice electrodes, will promote the development of high-performance RABs and other multivalent-ion batteries.

Methods

Materials

Aluminium trichloride ($AlCl_3$, 99.999%) was purchased from Sigma-Aldrich. 1-ethyl-3-methylimidazolium chloride (EMImCl, 99%) was obtained from Shanghai Chengjie Chemical Co., Ltd, China. Vanadium pentoxide (V_2O_5, 99.99% metals basis), aniline (99.5%, AR), ammonium molybdate tetrahydrate ($(NH_4)_6Mo_7O_{24}{\cdot}4H_2O$, AR), hexadecyl

trimethyl ammonium (CTAB, AR), and ammonium metavanadate (NH_4VO_3, AR) were supplied by Shanghai Aladdin Biochemical Technology Co. Ltd, China. Glass fiber filters (GF/A) were obtained from Whatman. Hydrochloric acid (HCl, AR) and iron(III) chloride hexahydrate ($FeCl_3$•$6H_2O$, ACS, Reag. Ph Eur) were bought from Sinopharm Chemical Reagent Co., Ltd, China. Aluminium foil (0.25 mm, annealed, 99.99%) and Mo foil (0.10 mm, metals basis, 99.95%, Alfa Aesar).

Synthesis of superlattice P-V_2O_5

Precisely 0.36 g of commerical V_2O_5 was weighed and dissolved in 60 mL of distilled water. Until completely dissolved, the mixture was transferred to an ice water bath and dripped 120 μL of aniline. Then, slowly dropwising a quantity of hydrochloric acid to adjust the pH of the solution (the PH vaule was ~2.5–3.0). After continuing to stir for 1.0 h, the homogeneous solution was poured into a reactor and maintained at 120 °C for 20 h. After the reaction, the product was washed several times with deionised water and ethanol and dried for 24 h. Finally, a dark green powder was obtained, that was, P-V_2O_5. In contrast, a series of hybrid PANI and V_2O_5 materials (P_x-V_2O_5) were prepared and the synthesis strategy was similar to P-V_2O_5, except the amount of aniline (x = 40, 180, 240, and 480 μL), named as P_1-V_2O_5, P_2-V_2O_5, P_3-V_2O_5, and P_4-V_2O_5.

Synthesis of superlattice V_2O_5-CTAB and V_2O_5-SDBS

0.175 g of NH_4VO_3 and 0.20 g of CTAB or SDBS were dissolved in 60 mL of anhydrous ethanol, and afterwards 1 mL of concentrated nitric acid was added. The solution was stirred for 30 min to obtain a homogeneous solution and transferred to a polybenzenes (PPL) reactor at 200 °C for 24 h, marked as V_2O_5-CTAB and V_2O_5-SDBS.

Synthesis of superlattice P-MoO_3

1 mL of aniline was dispersed in 99 mL of water, and afterwards the pH of the solution was adjusted to 0.5, denoted as solution A. Meanwhile, 0.002 mol of $(NH_4)_6Mo_7O_{24}$•$4H_2O$ and 0.007 mol of $FeCl_3$•$6H_2O$ were dissolved in 200 mL and 100 mL of distilled water, respectively, as solutions B and C. After the above-mentioned solutions were dispersed, C was slowly added to solutions A and B and stirred at room temperature for several days. Finally, the as-prepared product was filtered and dried to obtain the sample, named P-MoO_3.

Materials characterizations

The morphologies and element mapping of samples were characterized via SEM (SU8020) and TEM (FEI Talos F200X-G2). Cross-sectional TEM images of V_2O_5 and superlattice P-V_2O_5 were made by FEI Titan at 100 kV accelerating voltage. The crystal structure and diffraction peaks of the samples were acquired using XRD (Bruker, D8 Advance diffractometer). TG analysis (NETZSCH ST 449 F5/F3 Jupiter thermoanalyzer) was performed under air atmosphere from 25–500 °C with a heating rate of 5 °C min^{-1}. XPS spectra were obtained from a Thermo Fisher, ESCALAB 250 Xi, and the superlattice P-V_2O_5 samples were ion-etched with different etching times of 30 s, 1 min, and 2 min. Raman spectra were collected via the Renishaw instrument with a 532 nm laser. FT-IR spectra were measured on an IR spectrometer (Bruker Tensor-II FTIR, Germany). Atomic force microscope (AFM) and kelvin probe force microscopy (KPFM) images were acquired on multimode 8 (Bruker, Germany, tapping mode). The X-ray absorption fine structure spectra (XANES) spectra of V K-edge were performed at 1W1B station of Beijing Synchrotron Radiation Facility (BSRF).

Preparation of the electrodes

All the cathodes were prepared by mixing active material, ketjen black, and sodium carboxymethyl cellulose (CMC) at a weight ratio of 6:3:1 in deionized water in a mortar for 30 min to produce a slurry. Mo foil was also acted as a cathode current collector. The slurry was uniformly coated on a clean Mo foil via blade casting and then dried in a vacuum oven at 80 °C for 12 h to ensure the solvent fully removal. The as-prepared cathodes with mass loading around 1.0 mg cm^{-2} and 8 mm lateral dimensions were fabricated. The cells were assembled in an argon-filled glovebox (H_2O < 0.01 ppm, O_2 < 0.01 ppm).

Electrochemistry measurements

Electrochemical tests were performed at 25 °C via Swagelok-type cell. High-purity aluminium was used as anode, and glass fiber membrane was acted as separator, and the electrolyte was typical Lewis acidic ionic liquid (the molar ratio of $AlCl_3$ to EMImCl was 1.3:1). The anhydrous $AlCl_3$ (99.999%, Sigma-Aldrich) and EMImCl (99%, Shanghai Chengjie) were mixed under continually stirring 3.0 h in an argon atmosphere glovebox to form a homogeneous and transparent ionic liquid. Galvanostatic discharge/charge tests were conducted with a voltage range 0.25–2.25 V by a Neware battery test system based on active materials. Galvanostatic intermittent titration technique (GITT) profiles were obtained from pulses of 10 μA and interruption time for 20 min, and the CV curves were obtained using CHI440e workstation.

DFT simulations

The density functional theory (DFT) calculations were performed using a Castep module of Material Studio 2020[37]. The generalized gradient approximation (GGA) method with Perdew-Burke-Ernzerhof (PBE) function was employed to describe the interactions between the valence electrons and the ionic core[38,39]. The energy cut-off for the plane-wave basis set was 450 eV. The threshold values of the convergence criteria were specified as follows: 0.001 Å for maximum displacement, 0.03 eV $Å^{-1}$ for the maximum force, 0.05 GPa for the maximum stress, 10^{-5} eV/atom for energy, and 2.0×10^{-6} eV/atom for self-consistent field tolerance. The Brillouin zone integration was performed using a 2 × 2 × 1 k-mesh. The (002) surface of V_2O_5 was cleaved. Two layers (5 Å) of cell thickness were chosen to approximate the bulk properties. And then the interlamellar spacing of the two layers was adjusted to the experimentally reported value (4.37 Å). 15 Å vacuum space was implemented into the model to eliminate undesirable interactions between bottom side of the slab and the molecules. When dealing with V_2O_5 (002), it was required to generate 2 × 1 × 1 supercell of 80 atoms in order to do the appropriate calculations on the resulting information. Based on V_2O_5 (002), the superlattice P-V_2O_5 was build. The interlamellar spacing of the two layers for the superlattice P-V_2O_5 was 13.81 Å. Then polyaniline was added into the two layers of superlattice P-V_2O_5. When the optimization was completed, the density difference calculations were performed. Also, the diffusion barrier energy were located utilizing the well-known linear synchronous transit (LST) and quadratic synchronous transit (QST) methods. The binding energy (ΔE) was calculated as the Eq. (1):

$$\Delta E = (E_{total} - E_1 - E_2) \quad (1)$$

where the E_{total} is the energy of the optimized system, E_1 is the energy of an optimized $AlCl_4^-$ within a 10 × 10 × 10 Å box, E_2 is the energy of the bare surface.

Binding energy calculations related to the open-circuit voltage were performed by the Vienna *ab*-initio simulation package (VASP)[40,41]. The projector-augmented wave (PAW) pseudopotential and a plane-wave basis set with a 500 eV cutoff energy were used in the calculation[42]. The GGA-PBE functions were carried out to describe the exchange-correlation potentials[38]. A Monkhorst-Pack scheme with k-spacing of 2π × 0.030 $Å^{-1}$ was used for Brillouin zone sampling[43]. The convergence tolerance was set to 10^{-5} eV and 0.01 eV $Å^{-1}$ for total energy and force, respectively.

Finite element modeling

The ion flux boundary of $AlCl_4^-$ was the interface with the superlattice P-V_2O_5[44]. In spherical coordinates, the diffusion of $AlCl_4^-$ ions in the

superlattice P-V_2O_5 was determined by Eq. (2):

$$\frac{\partial c}{\partial t} + \frac{1}{r^2}\frac{\partial (r^2 \mathbf{J})}{\partial r} = 0 \tag{2}$$

Where, c is the molar concentration of $AlCl_4^-$ ion, the flux is determined by $\mathbf{J} = Dc\nabla\mu/(R_gT)$, D, μ, R_g, and T are the diffusion coefficient, chemical potential, ideal gas constant and temperature of $AlCl_4^-$ ion, respectively. Therefore, the chemical potential can be further expressed as:

$$\mu = \mu_0 + R_g T \ln c \tag{3}$$

Where μ_0 is the reference chemical potential.

$$\frac{\partial c}{\partial t} = \frac{1}{r^2}\frac{\partial}{\partial r}\left\{Dr^2\left(\frac{\partial c}{\partial r}\right)\right\} \tag{4}$$

Driven by the chemical potential gradient, it was assumed that the intercalating process of $AlCl_4^-$ ions on the surface occurs in a galvanostatic stage, and the corresponding initial conditions and boundary condition were expressed as follows:

$$\begin{gathered} c = c_0\,(t = 0) \\ -\mathbf{n}\cdot\mathbf{J}|_{r=0} = 0, -\mathbf{n}\cdot\mathbf{J}|_{r=a} = \frac{i_n}{F} \end{gathered} \tag{5}$$

Where, the particle surface current density: $i_n = \frac{nc_m Fa}{10800}$, c_O is the initial concentration of $AlCl_4^-$ in the superlattice P-V_2O_5, c_m is the saturation concentration, and n is the charge and discharge ratio.

As a linear elastic material, the strain relationship of superlattice P-V_2O_5 was shown as follows:

$$\begin{gathered} \varepsilon_{ij}^{total} = \varepsilon_{ij}^{e} + \varepsilon_{ij}^{d} \\ \varepsilon_{ij}^{d} = \frac{1}{3}\Omega c \delta_{ij} \end{gathered} \tag{6}$$

Where, ε_{ij}^{total} denotes the total strain, ε_{ij}^{d} is the diffusion-induced strain generated by the $AlCl_4^-$ ion embedding process, Ω is the partial molar volume of $AlCl_4^-$ ion, ε_{ij}^{e} is the elastic strain, determined by Eq. (7).

$$\varepsilon_{ij}^{e} = \frac{1}{E}[(1+\upsilon)\sigma_{ij} - \upsilon\sigma_{kk}\delta_{ij}] \tag{7}$$

Where E, υ, σ_{ij}, and δ_{ij} represent Young's modulus, Poisson's ratio, stress tensor, and Kronecker symbol of superlattice P-V_2O_5, respectively.

Data availability

Source data are provided in this paper. Extra data are also available from the corresponding author upon request. Source data are provided with this paper.

References

1. Park, G.-T. et al. Introducing high-valence elements into cobalt-free layered cathodes for practical lithium-ion batteries. *Nat. Energy* **7**, 946–954 (2022).
2. Armand, M. & Tarascon, J. M. Building better batteries. *Nature* **451**, 652–657 (2008).
3. Ng, K. L., Amrithraj, B. & Azimi, G. Nonaqueous rechargeable aluminum batteries. *Joule* **6**, 134–170 (2022).
4. Zhang, J. et al. Self-adaptive re-organization enables polythiophene as an extraordinary cathode material for aluminum-ion batteries with a cycle life of 100,000 cycles. *Angew. Chem. Int. Ed.* **135**, e202215408 (2023).
5. Faegh, E., Ng, B., Hayman, D. & Mustain, W. E. Practical assessment of the performance of aluminium battery technologies. *Nat. Energy* **6**, 21–29 (2021).
6. Lin, M. C. et al. An ultrafast rechargeable aluminium-ion battery. *Nature* **520**, 325–328 (2015).
7. Park, Y., Lee, D., Kim, J., Lee, G. & Tak, Y. Fast charging with high capacity for aluminum rechargeable batteries using organic additive in an ionic liquid electrolyte. *Phys. Chem. Chem. Phys.* **22**, 27525–27528 (2020).
8. Tu, J. et al. Nonaqueous rechargeable aluminum batteries: progresses, challenges, and perspectives. *Chem. Rev.* **121**, 4903–4961 (2021).
9. Wang, C. et al. Monolayer atomic crystal molecular superlattices. *Nature* **555**, 231–236 (2018).
10. Hu, L. et al. Unlocking the charge doping effect in softly intercalated ultrathin ferromagnetic superlattice. *eScience* **3**, 100117 (2023).
11. Ma, X. et al. Organic-inorganic hybrid cathode with dual energy storage mechanism for ultra-high-rate and ultra-long-life aqueous zinc-ion batteries. *Adv. Mater.* **34**, 2105452 (2021).
12. Hanada, N. et al. X-ray absorption spectroscopic study on valence state and local atomic structure of transition metal oxides doped in MgH_2. *J. Phys. Chem. C.* **113**, 13450–13455 (2009).
13. Yue, X.-Y. et al. Sputtered MoN nanolayer as a multifunctional polysulfide catalyst for high-performance lithium-sulfur batteries. *eScience* **2**, 329–338 (2022).
14. Wang, X. et al. Two-dimensional amorphous TiO_2 nanosheets enabling high-efficiency photoinduced charge transfer for excellent SERS activity. *J. Am. Chem. Soc.* **141**, 5856–5862 (2019).
15. Senguttuvan, P. et al. A high power rechargeable nonaqueous multivalent Zn/V_2O_5 battery. *Adv. Energy Mater.* **6**, 1600826 (2016).
16. Wang, Y., Shi, X., Wang, J., Liu, X. & Lu, X. Nanobelt-like vanadium dioxide with three-dimensional interconnected tunnel structure enables ultrafast Al-ion storage. *Mater. Today Energy* **19**, 100578 (2021).
17. Cui, F. et al. Superlattice-stabilized WSe_2 cathode for rechargeable aluminum batteries. *Small Methods* **6**, 2201281 (2022).
18. Lv, W., Wu, G., Li, X., Li, J. & Li, Z. Two-dimensional V_2C@Se (MXene) composite cathode material for high-performance rechargeable aluminum batteries. *Energy Stor. Mater.* **46**, 138–146 (2022).
19. Yang, K. et al. Locally ordered graphitized carbon cathodes for high-capacity dual-ion batteries. *Angew. Chem. Int. Ed.* **60**, 6326–6332 (2021).
20. Babar, M. et al. Effect of disorder and doping on electronic structure and diffusion properties of $Li_3V_2O_5$. *J. Phys. Chem. C.* **126**, 15549–15557 (2022).
21. Muralidharan, N. et al. Tunable mechanochemistry of lithium battery electrodes. *ACS Nano* **11**, 6243–6251 (2017).
22. Gu, S. et al. Confirming reversible Al^{3+} storage mechanism through intercalation of Al^{3+} into V_2O_5 nanowires in a rechargeable aluminum battery. *Energy Stor. Mater.* **6**, 9–17 (2017).
23. Shi, J., Zhang, J. & Guo, J. Avoiding pitfalls in rechargeable aluminum batteries research. *ACS Energy Lett.* **4**, 2124–2129 (2019).
24. Wang, S., Huang, S., Yao, M., Zhang, Y. & Niu, Z. Engineering active sites of polyaniline for $AlCl_2^+$ storage in an aluminum-ion battery. *Angew. Chem. Int. Ed.* **59**, 11800 (2020).
25. Koketsu, T. et al. Reversible magnesium and aluminium ions insertion in cation-deficient anatase TiO_2. *Nat. Mater.* **16**, 1142 (2017).
26. Lin, Z. J. et al. Amorphous anion-rich titanium polysulfides for aluminum-ion batteries. *Sci. Adv.* **7**, eabg6314 (2021).
27. Li, H. et al. Reversible electrochemical oxidation of sulfur in ionic liquid for high-voltage Al-S batteries. *Nat. Commun.* **12**, 5714 (2021).
28. Meng, J. et al. A solution-to-solid conversion chemistry enables ultrafast-charging and long-lived molten salt aluminium batteries. *Nat. Commun.* **14**, 3909 (2023).

29. Liu, Y. et al. Redox-bipolar polyimide two-dimensional covalent organic framework cathodes for durable aluminium batteries. *Angew. Chem. Int. Ed.* **62**, e202306091 (2023).
30. Kim, D. J. et al. Rechargeable aluminium organic batteries. *Nat. Energy* **4**, 51–59 (2018).
31. Yoo, D. J., Heeney, M., Glocklhofer, F. & Choi, J. W. Tetradiketone macrocycle for divalent aluminium ion batteries. *Nat. Commun.* **12**, 2386 (2021).
32. Wang, D. Y. et al. Advanced rechargeable aluminium ion battery with a high-quality natural graphite cathode. *Nat. Commun.* **8**, 14283 (2017).
33. Diem, A. M., Bill, J. & Burghard, Z. Creasing highly porous V_2O_5 scaffolds for high energy density aluminum-ion batteries. *ACS Appl. Energy Mater.* **3**, 4033–4042 (2020).
34. Wang, H. Z. et al. Revealing the multiple cathodic and anodic involved charge storage mechanism in an $FeSe_2$ cathode for aluminium-ion batteries by in situ magnetometry. *Energy Environ. Sci.* **15**, 311–319 (2022).
35. Yuan, Z., Lin, Q., Li, Y., Han, W. & Wang, L. Effects of multiple ion reactions based on a $CoSe_2$/MXene cathode in aluminum-ion batteries. *Adv. Mater.* **35**, e2211527 (2023).
36. Pang, Q. et al. Fast-charging aluminium-chalcogen batteries resistant to dendritic shorting. *Nature* **608**, 704–711 (2022).
37. Segall, M. D. et al. First-principles simulation: ideas, illustrations and the CASTEP code. *J. Phys. Condens* **14**, 2717–2744 (2002).
38. Perdew, J. P., Burke, K. & Ernzerhof, M. Generalized gradient approximation made simple. *Phys. Rev. Lett.* **77**, 3865–3868 (1996).
39. Vanderbilt, D. Soft self-consistent pseudopotentials in a generalized eigenvalue formalism. *Phys. Rev. B* **41**, 7892–7895 (1990).
40. Kresse, G. & Hafner, J. Ab initio molecular-dynamics simulation of the liquid-metal-amorphous-semiconductor transition in germanium. *Phys. Rev. B Condens. Matter* **49**, 14251–14269 (1994).
41. Kresse, G. & Hafner, J. Ab initio molecular dynamics for liquid metals. *Phys. Rev. B Condens. Matter* **47**, 558–561 (1993).
42. Blochl, P. E. Projector augmented-wave method. *Phys. Rev. B Condens. Matter* **50**, 17953–17979 (1994).
43. Chadi, D. J. Special points for Brillouin-zone integrations. *Phys. Rev. B* **16**, 1746–1747 (1977).
44. Wu, B. & Lu, W. Mechanical modeling of particles with active core-shell structures for lithium-ion battery electrodes. *J. Phys. Chem. C.* **121**, 19022–19030 (2017).

Acknowledgements

We appreciate Lirong Zheng (Beijing Synchrotron Radiation Facility, Chinese Academy of Sciences) for the discussion of the XAFS data, and the support from Taifeng Lin in School of Chemistry and Life Science, Beijing University of Technology. This research was financially supported by the National Natural Science Foundation of China (No. 52374295, and 52130407), National Key Research and Development Program of China (2022YFB2402400, and 2022YFB3705403), Young Elite Scientists Sponsorship Program by CAST, Beijing Municipal Great Wall Scholar Training Plan Project (CIT&TCD20190307), Beijing Municipal Commission of Education (KZ20231000509, KZ202210005003), and Beijing Natural Science Foundation (Z210016).

Author contributions

Y.X.H. put forward the idea. H.Y.L., S.J.P., and Y.X.H. supervised the experiment. F.Y.C. and Y.X.H. conceived and designed this work. J.Z.L. and C.L. carried out the computations. C.Z.L., C.H.S., A.M.H, and K.D. assisted in data measurements. Y.X.H., H.Y.L., and J.S.W. reviewed the paper. F.Y.C. and Y.X.H. prepared the manuscript. Y.X.H., H.Y.L. and J.Z.L. revised the manuscript.

Competing interests

The authors declare no competing interests.

Additional information

Supplementary information The online version contains supplementary material available at https://doi.org/10.1038/s41467-024-51570-9.

Correspondence and requests for materials should be addressed to Hongyi Li, Shengjie Peng or Yuxiang Hu.

Peer review information *Nature Communications* thanks Joseph Montoya, Dong-Joo Yoo and the other, anonymous, reviewer(s) for their contribution to the peer review of this work. A peer review file is available.